Paper AAS 05-341



# Discrete Nonlinear Optimal Control of S/C Formations Near the $L_1$ and $L_2$ Points of the Sun-Earth/Moon System

B. G. Marchand and K. C. Howell
School of Aeronautics and Astronautics
Purdue University
315 N. Grant Street
West Lafayette, IN 47907-2023

J. T. Betts
Technical Fellow
Mathematics and Engineering Analysis
The Boeing Company
P.O. Box 3707, MS 7L-21
Seattle, WA 98124-2207

**AAS/AIAA Astrodynamics Specialists Conference**

**Lake Tahoe, CA, August 7-11, 2005**

**AAS Publications Office, P.O. Box 28130, San Diego, CA 92198**

# Discrete Nonlinear Optimal Control of S/C Formations Near the L1 and L2 Points of the Sun-Earth/Moon System

B. G. Marchand* and K. C. Howell†
Purdue University

and

J. T. Betts‡
The Boeing Company

Spacecraft formations near the libration points of the Sun-Earth/Moon system represent one option currently under consideration for applications to space based interferometry. This type of mission often requires precision tracking from the vehicles in the formation. However, past studies reveal that the dynamically sensitive nature of this region of space presents a number of unique challenges in this respect. For instance, the addition of thrust constraints into the design problem can significantly limit the level of positional accuracy that is achievable. The focus of this investigation is the application of discrete nonlinear optimal control to the constrained formation keeping problem.

## INTRODUCTION

A formation of vehicles, here, is characterized by one primary or central vehicle defined as the chief spacecraft. The remaining vehicles in the formation, then, are termed deputies. Within this context, "formation flight" is defined as a number of deputies commanded to follow some prescribed nominal path relative to the chief spacecraft. Note that the chief spacecraft need not be an actual vehicle. It may also represent a generic reference point relative to which the dynamical characteristics of the deputy are measured. In this study, it is assumed that the reference chief vehicle evolves along a natural trajectory arc, such as a halo orbit or Lissajous trajectory, near the L1 or L2 libration point. This, in theory, implies that no control effort is required to maintain the path of the reference vehicle since the solution exists naturally. Subsequently, the deputy vehicles evolve along their paths, relative to the reference vehicle, as the chief spacecraft evolves along its orbit.

The dynamical sensitivity that is characteristic of the region near the libration points associated with any three-body system, combined with the path constraints usually imposed on an envisioned configuration, makes formation keeping and deployment an interesting and challenging problem. Although some preliminary analyses have already been completed [1-17], a better understanding of formation keeping in the presence of control input constraints is still necessary. Of course, an added difficulty, inherent to this dynamical regime, is that no analytical solution for the reference path of a spacecraft exists. Although some approximations are available, any analysis involving formation flight in multi-body systems is still strongly dependent on numerical methods.

* Visiting Assistant Professor, School of Aeronautics and Astronautics, Purdue University, West Lafayette, IN 47907-2023
† Professor, School of Aeronautics and Astronautics, Purdue University, West Lafayette, IN 47907-2023
‡ Technical Fellow, Mathematics and Engineering Analysis, The Boeing Company, Seattle, WA 98124-2207

In this investigation, the design and control of spacecraft formations is accomplished through nonlinear optimal control methods. The theoretical foundation for this approach is based on the Euler-Lagrange optimality conditions [18]. These optimality conditions are, of course, derived from the calculus of variations. Thus, the process is not self-starting since an adequate initial guess is required. In a dynamically sensitive regime, the success of this approach is strongly dependent on the initial guess and how close this solution is to the optimal trajectory.

The numerical determination of the optimal control solution is accomplished in one of two ways. First, the trajectory is divided into segments at nodes or grid points. Then, the state equations and constraints that describe the problem are discretized accordingly. In the first method, the determination of the optimal solution is based on either impulsive maneuvers at each node or constant thrust arcs between grid points. The second method allows for both of these options as well as the determination of optimal arcs involving continuous control. Some fundamental examples are selected in both cases. The results of this study represent the foundation of future efforts involving constrained formation keeping near the libration points.

## DYNAMICAL MODEL

### Circular Restricted Three-Body Model

In this study, the central spacecraft is termed "chief" while all other vehicles in the formation are denoted as "deputies". In the CR3BP, the motion of the chief S/C is described in terms of rotating coordinates ($R$) relative to the barycenter ($B$) of the system primaries (SEM system). In this frame, the rotating $x$-axis is directed from the Sun towards the Earth-Moon barycenter, as illustrated in Figure 1. The $z$-axis is normal to the plane of motion of the primaries, and the $y$-axis completes the right-handed triad. Alternatively, in the ephemeris model, the frame of reference is inertial ($I$) and Earth centered ($P_2$).

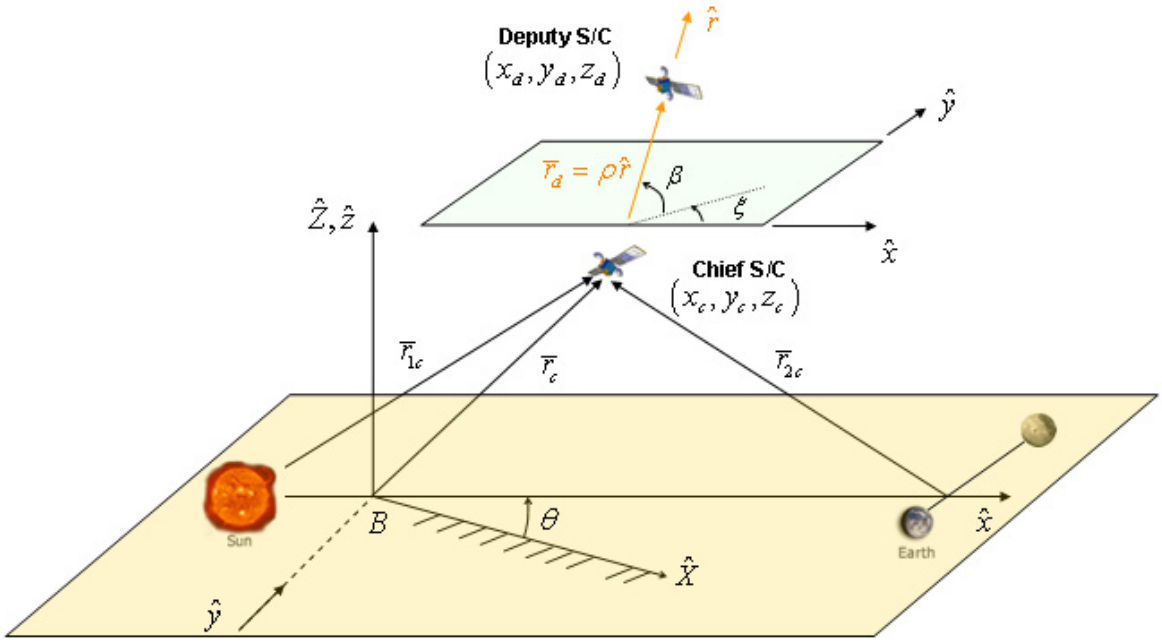


**Figure 1 - Two S/C Formation in the Sun-Earth/Moon CR3BP**

In either formulation, equations of motion for either the chief or the deputy vehicle, relative to a reference point $Q$ ($B$ or $P_2$), can be expressed, in a general form, as

$$\begin{aligned} \ddot{\bar{r}}(t) &= \bar{f}\left(\bar{r}_d(t), \dot{\bar{r}}_d(t)\right) - \bar{f}\left(\bar{r}_c(t), \dot{\bar{r}}_c(t)\right) + \bar{u}_d(t) - \bar{u}_c(t), \\ \ddot{\bar{r}}(t) &= \Delta\bar{f}\left(\bar{r}(t), \dot{\bar{r}}(t), \bar{r}_c(t), \dot{\bar{r}}_c(t)\right) + \Delta\bar{u}(t). \end{aligned} \tag{1}$$

The subscript "c" indicates that the function is associated with the chief spacecraft while the subscript "d" implies evaluation along the path of the deputy. The position vectors $\bar{r}_c$ and $\bar{r}_d$, then, locate the chief and deputy vehicles relative to the reference point $Q$, respectively. The vector $\bar{r} = \bar{r}_d - \bar{r}_c = [x, y, z]^T$ locates the deputy spacecraft relative to the chief vehicle. The quantity $\Delta\bar{f} = \left[\Delta f_x, \Delta f_y, \Delta f_z\right]^T$ represents the vector sum of the net forcing terms (gravity + solar radiation pressure) acting on the vehicles as well as any kinematic terms that may be present due to the working frame associated with the specified formulation.

In the present investigation, the chief spacecraft is assumed to evolve along a naturally existing solution such that $\bar{u}_c(t) = 0$, hence $\Delta\bar{u}(t) = \bar{u}_d(t)$. In this study, the effects of solar radiation pressure (SRP) are only considered in the ephemeris model and the form of the SRP force is consistent with the definition stated by McInnes [19].

**Nonlinear Optimal Control for Formation Keeping**

In previous investigations, Howell and Marchand [14-17] propose a variety of impulsive targeter methods, including a modified Floquet controller, to establish bounded formations near an L1 or L2 halo orbit in the Sun-Earth/Moon system. Among these, position and radial targeters [16] are designed to enforce a non-natural relative position between the vehicles in the formation. The Floquet method [17], on the other hand, is mainly employed to establish natural relative orbits for the deputy vehicles. Thus, in theory, no control effort is required to enforce these trajectories.

Presently, these methodologies are employed to assist in the construction of adequate startup trajectories for the optimal formation keeping problem. The ultimate goal of the optimization procedure is to minimize the propulsive cost, within the bounds established by the thrusters and the mission constraints, as well as the deviations from the specified nominal path. A suitable startup solution is crucial since the optimal control techniques employed are based on the calculus of variations. By definition, this approach assumes that the initial guess exists in the vicinity of the optimal solution. In a dynamically sensitive regime, such as the multi-body problem, establishing good initial approximations is crucial to the convergence of the optimization algorithm.

Two solution methods are presented here. Both methodologies require the discretization of the state equations. In the first approach, the states and gradient matrices at each node are determined through numerical integration. The solution of the optimal control problem is then accomplished through a subspace trust region method that requires knowledge of the gradient (Jacobian) at each node along the trajectory. Alternatively, the second method employs an approximation of the continuous system based on a Hermite-Simpson discretization. Then, the solution to the optimal control problem is obtained through the Sparse Optimal Control Software (SOCS), developed by Betts [20-24].

SOCS is a collection of FORTRAN 77 subroutines capable of solving optimal control problems. The package implements a direct transcription method to convert the continuous control problem into a discrete approximation. The discretization yields a finite dimensional sparse nonlinear programming problem that can be solved using sequential quadratic programming. Numerical procedures to improve the accuracy of the discretization by mesh refinement are implemented in the package.

Examples are presented here to demonstrate the merit and feasibility of both methodologies. Of course, the ultimate goal of this approach is the solution of the constrained formation keeping problem; that is, formation keeping in the presence of control input upper and lower bounds. Later stages of this investigation also seek to establish the position accuracy that is physically achievable, near the libration points, in the presence of such hardware constraints.

Method #1: Optimal Control by Partial Discretization

Consider a discrete nonlinear map,

$$\bar{y}(t_j) = \bar{F}\left[\bar{y}(t_{j-1}), \bar{u}(t_{j-1}), t_{j-1}\right], \tag{2}$$

subject to a fixed initial state ( $\bar{y}_i$ ),

$$\bar{y}(t_0) = \bar{y}_0 = \bar{y}_i. \tag{3}$$

Note that this map is directly related to the original nonlinear equations of motion through a simple integration over the segment defined by $t_{j-1} \le t \le t_j$ ,

$$\bar{y}(t_j) = \bar{y}(t_{j-1}) + \int_{t_{j-1}}^{t_j} \bar{F}\left(\bar{y}(t), \bar{u}(t), t\right) dt. \tag{4}$$

Suppose the trajectory is divided into $N$ nodes and $N-1$ segments such that $t_i = t_0 < t_1 < \ldots < t_N = t_f$ , where $t_i$ and $t_f$ represent the initial and final times, respectively. The states at each node, in this case, are obtained through a sequential numerical integration process. The control options include application of an impulsive input at the start of each segment or application of constant thrust over the length of each segment. Considering these alternatives, let $J$ denote a scalar cost function of the states and inputs at each node along the trajectory. The goal, then, is to identify the sequence of control inputs that will minimize

$$J = \phi\left(\bar{y}(t_N)\right) + \sum_{j=1}^{N} L\left[\bar{y}(t_{j-1}), \bar{u}(t_{j-1}), t_{j-1}\right]. \tag{5}$$

This cost index, stated in the traditional form of Bolza, consists of two parts. The first term, $\phi\left(\bar{y}(t_N)\right)$, represents a nonlinear function of the state at the end of the trajectory. The remaining terms, then, are contributions associated with the state and control input at each node along the trajectory. In addition, the cost index is subject to a series of vector equality constraints that include the initial condition along the trajectory and the equations of motion. Although the Bolza formulation is intuitive, simplifying the cost index to Mayer form is most convenient from a computational perspective. To that end, the $n$ -dimensional state vector $\bar{y}$ is augmented by one variable,

$$y_{n+1}(t_j) = y_{n+1}(t_{j-1}) + L\left[\bar{y}_{j-1}, \bar{u}_{j-1}, t_{j-1}\right]. \tag{6}$$

It is clear, then, that

$$y_{n+1}(t_N) = \sum_{j=1}^{N} L\left[\bar{y}_{j-1}, \bar{u}_{j-1}, t_{j-1}\right]. \tag{7}$$

Now, the cost function $J$ , in Equation (5) is reduced to the form of Mayer,

$$J = \tilde{\phi}\left(\tilde{y}_N\right), \tag{8}$$

where

$$\tilde{\phi} = \phi\left(\bar{y}_N\right) + y_{n+1}(t_N). \tag{9}$$

Let $\tilde{F}\left(\tilde{y}_i, \bar{u}_i, t_i\right)$ denote the augmented nonlinear map,

$$\tilde{y}_j = \tilde{F}\left(t_{j-1}, \tilde{y}_{j-1}, \bar{u}_{j-1}\right) = \begin{bmatrix} \bar{F}\left(\bar{y}_{j-1}, \bar{u}_{j-1}, t_{j-1}\right) \\ y_{n+1}\left(t_{j-1}\right) + L\left[\bar{y}_{j-1}, \bar{u}_{j-1}, t_{j-1}\right] \end{bmatrix}. \tag{10}$$

The optimality conditions for this augmented system, as defined by Bryson [18], are subsequently determined as

$$\tilde{\lambda}_N^T = \frac{\partial \tilde{\phi}\left(\tilde{y}_N\right)}{\partial \tilde{y}_N}, \tag{11}$$

$$\tilde{\lambda}_{j-1}^T = \tilde{\lambda}_j^T \frac{\partial \tilde{F}_{j-1}}{\partial \tilde{y}_{j-1}}, \tag{12}$$

$$\frac{\partial \tilde{H}_{j-1}}{\partial \bar{u}_{j-1}} = \tilde{\lambda}_j^T \frac{\partial \tilde{F}_{j-1}}{\partial \bar{u}_{j-1}}. \tag{13}$$

The optimal solution is identified using a subspace trust region method, based on the interior-reflective Newton method described by Coleman and Li [25-26]. Each iteration involves the approximate solution of a large linear system using the method of preconditioned conjugate gradients. This particular method attempts to find a minimum of a scalar function, $J$, of several variables $\bar{u}_{in}$, based on some initial estimate and analytically available gradients, $H_{\bar{u}_{in}}$, determined from Equation (13). To solve the optimal control problem numerically, the control vector and the associated gradient at every node, are each reshaped into a single vector with $3(N-1)$ components such that

$$\bar{u}_{in}(3(j-1)+1:3(j-1)+3) = [u_x(t_{j-1}),\ u_y(t_{j-1}),\ u_z(t_{j-1})], \tag{14}$$

and

$$\bar{H}_{\bar{u}_{in}}(3(j-1)+1:3(j-1)+3) = [H_{u_x}(t_{j-1}), H_{u_y}(t_{j-1}), H_{u_z}(t_{j-1})], \tag{15}$$

for $j = 1, \ldots, N$. In this case $H_{u_x} = \partial H / \partial u_x$, $H_{u_y} = \partial H / \partial u_y$, and $H_{u_z} = \partial H / \partial u_z$.

Note that the usefulness and success of the above procedure is predicated on two assumptions;

- the availability of an exact discrete map, such as that in Equation (2), and
- the availability of an exact form for the gradients in Equations (12) and (13).

If both of these conditions are true, then this procedure essentially converts a functional optimization problem into a parameter optimization problem. However, neither of these assumptions hold in the gravitational *n*-body problem, where no exact closed-form solutions exist. One way of dealing with this issue is to employ a partial discretization approach, where the states at each node are numerically integrated. As demonstrated in the following sections, depending on the problem formulation, the gradients may also be numerically integrated along with the equations of motion by introducing an augmented system of equations into the numerical solution process.

*Applications to Formation Flight Near the Libration Points*

Targeter algorithms [16-17] seek to enforce some nominal state, or constraint, at the end of a trajectory segment. Numerically, this is accomplished by applying an impulsive maneuver at the beginning of the segment. The targeter identifies the maneuver required to achieve the desired end state or constraint. This type of formulation, however, does not offer any control over the deviations incurred between maneuvers.

In fact, in the formation keeping problem, it may be most desirable to minimize the total error over the length of the mission, or segment, rather than just the end state error. In this case, the cost index may be formulated as a sum of quadrature functions,

$$y_{n+1}(t_N) = \sum_{j=1}^{N} \int_{t_{j-1}}^{t_j} \tilde{L}[\bar{y}, \bar{u}, t]\, dt. \tag{16}$$

For this type of system, the partial derivatives are easily determined from knowledge of the linear system dynamics. To illustrate, let

$$\dot{\tilde{y}} = \tilde{f}(t, \tilde{y}, \tilde{u}) = \begin{bmatrix} \bar{f}(t, \tilde{y}, \bar{u}) \\ \tilde{L}(t, \tilde{y}, \bar{u}) \end{bmatrix}, \tag{17}$$

represent the augmented state equations to be numerically integrated. This system is subject to initial conditions of the form

$$\tilde{y}(0) = \begin{bmatrix} \bar{y}_0 \\ 0 \end{bmatrix}. \tag{18}$$

Linearization of the system in Equation (17) yields

$$\delta\dot{\tilde{y}}(t) = \tilde{A}(t)\delta\tilde{y}(t) + \tilde{B}(t)\delta\bar{u}(t), \tag{19}$$

where

$$\tilde{A}(t) = \begin{bmatrix} \dfrac{\partial \bar{f}}{\partial \bar{y}} & \dfrac{\partial \bar{f}}{\partial y_{n+1}} \\ \dfrac{\partial \tilde{L}}{\partial \bar{y}} & \dfrac{\partial \tilde{L}}{\partial y_{n+1}} \end{bmatrix} = \begin{bmatrix} A(t) & 0 \\ \dfrac{\partial \tilde{L}}{\partial \bar{y}} & 0 \end{bmatrix}, \tag{20}$$

and

$$\tilde{B} = \begin{bmatrix} 0_3 \\ I_3 \\ 0 \end{bmatrix}. \tag{21}$$

The solution to the linear system in Equation (19) is known to be of the form,

$$\delta\tilde{y}_j^- = \tilde{\Phi}(t_j, t_{j-1})\delta\tilde{y}_{j-1}^+ + \int_{t_{j-1}}^{t_j} \tilde{\Phi}(t, \tau)\tilde{B}(\tau)\delta\bar{u}(\tau)\, d\tau, \tag{22}$$

where $\tilde{\Phi}(t_j, t_{j-1})$ is the state transition matrix, for the $j^{th}$ segment, in the augmented nonlinear system. This matrix is determined by numerically integrating the following,

$$\dot{\tilde{\Phi}}(t, t_{j-1}) = \tilde{A}(t)\tilde{\Phi}(t, t_{j-1}), \tag{23}$$

subject to $\tilde{\Phi}(t_{j-1}, t_{j-1}) = I_{(n+1)}$. In Equation (22), the superscript '+' denotes initial conditions at the start of a numerically integrated segment while the '$-$' represents the numerically integrated state at the end of a segment. As previously discussed, there are two ways to implement a discrete control approach; impulsive control or constant thrust arcs.

The choice of control methodology determines how the control gradient in Equation (13) is computed. Of course, the partial derivative in Equation (12) is simply the state transition matrix,

$$\frac{\partial \tilde{F}_{j-1}}{\partial \tilde{y}_{j-1}} = \tilde{\Phi}\left(t_j, t_{j-1}\right), \tag{24}$$

regardless of the control methodology implemented.

*Impulsive Control*

If an impulsive control algorithm is sought, the integral term in Equation (22) vanishes and the resulting solution can be rewritten as follows,

$$\begin{aligned} \delta \tilde{y}_j^- &= \tilde{\Phi}\left(t_j, t_{j-1}\right)\delta \tilde{y}_{j-1}^+, \\ &= \tilde{\Phi}\left(t_j, t_{j-1}\right)\left(\delta \tilde{y}_{j-1}^- + \tilde{B}\Delta \overline{V}_{j-1}\right), \\ &= \tilde{\Phi}\left(t_j, t_{j-1}\right)\delta \tilde{y}_{j-1}^- + \tilde{\Phi}\left(t_j, t_{j-1}\right)\tilde{B}\Delta \overline{V}_{j-1}. \end{aligned} \tag{25}$$

The control input, in this case, is denoted by an impulsive maneuver ( $\Delta \overline{V}_{j-1}$ ). Equation (25) implies that the end state of the previous segment, after applying an impulsive maneuver, becomes the initial state at the beginning of the next segment. Note, from Equation (25), that

$$\frac{\partial \tilde{F}_{j-1}}{\partial \overline{u}_{j-1}} = \tilde{\Phi}\left(t_j, t_{j-1}\right)\tilde{B}. \tag{26}$$

The partial derivatives in Equations (24) and (26) are employed in evaluating the optimality conditions in Equations (12) and (13).

*Constant Thrust Arcs*

If, instead, constant thrusting over the length of each segment is desired, the determination of the control gradient, numerically, requires some additional consideration. In this case, the control input under the integral in Equation (22) is constant. Thus, the solution to the linear system is given by

$$\delta \tilde{y}_j^- = \tilde{\Phi}\left(t_j, t_{j-1}\right)\delta \tilde{y}_{j-1}^+ + \left[\int_{t_{j-1}}^{t_j} \tilde{\Phi}\left(t, \tau\right)\tilde{B}\left(\tau\right)d\tau\right]\delta \overline{u}_{j-1}. \tag{27}$$

Note that this expression may also be written as follows,

$$\delta \tilde{y}_j^- = \left(\frac{\partial \tilde{F}_{j-1}}{\partial \tilde{y}_{j-1}}\right)\delta \tilde{y}_{j-1}^+ + \left(\frac{\partial \tilde{F}_{j-1}}{\partial \overline{u}_{j-1}}\right)\delta \overline{u}_{j-1}, \tag{28}$$

where

$$\frac{\partial \tilde{F}_{j-1}}{\partial \tilde{y}_{j-1}} = \tilde{\Phi}\left(t_j, t_{j-1}\right), \tag{29}$$

and

$$\frac{\partial \tilde{F}_{j-1}}{\partial \overline{u}_{j-1}} = \int_{t_{j-1}}^{t_j} \tilde{\Phi}\left(t, \tau\right)\tilde{B}\left(\tau\right)d\tau. \tag{30}$$

The matrix $\tilde{\Phi}(t,\tau)$ is not actually available directly from the numerical integration. However, it can be computed at each instant in time based on the properties of the state transition matrix,

$$\tilde{\Phi}\left(t,t_{j-1}\right)=\tilde{\Phi}(t,\tau)\tilde{\Phi}\left(\tau,t_{j-1}\right). \tag{31}$$

From Equation (31), it is apparent that

$$\tilde{\Phi}(t,\tau)=\tilde{\Phi}\left(t,t_{j-1}\right)\tilde{\Phi}\left(\tau,t_{j-1}\right)^{-1}. \tag{32}$$

Substitution of Equation (32) into (30) reveals that the control gradient may be determined as

$$\frac{\partial \tilde{F}_{j-1}}{\partial \overline{u}_{j-1}}=\tilde{\Phi}\left(t,t_{j-1}\right)\int_{t_{j-1}}^{t}\tilde{\Phi}\left(\tau,t_{j-1}\right)^{-1}\tilde{B}(\tau)\,d\tau. \tag{33}$$

Thus, solving the optimal control problem for constant thrusting requires that Equations (17) and (23) be numerically integrated along with

$$\tilde{\tilde{\Phi}}^{*}\left(t,t_{j-1}\right)=\tilde{\Phi}\left(t,t_{j-1}\right)^{-1}\tilde{B}(t). \tag{34}$$

In the above expression, $\tilde{\Phi}^{*}$ is an $(n+1)\times 3$ matrix subject to $\tilde{\Phi}^{*}\left(t_{j-1},t_{j-1}\right)=0$.

Note that both of these formulations, involving optimal impulsive and constant thrust solutions, are applicable in general. These formulations are particularly useful when an exact mapping for the trajectory, such as that in Equation (2), is not available, and the user must therefore rely on numerically integrated trajectories. Indeed, the above formulations work well when the dynamical behavior of the system is relatively simple. However, as previously mentioned, some complications may arise when dealing with systems as dynamically complex as the *n*-body problem.

*Examples*

In the following examples, the optimization problem is approached from two different perspectives. In the "global" approach, the control sequence is optimized across all segments simultaneously. Note that the term "global" is used loosely and it is NOT meant to imply that the resulting solution is itself globally optimal. Since the optimality conditions are based on the calculus of variations, any optimal solution that is identified through this approach exists in the vicinity of the initial guess and, thus, represents a local optimal. No further conclusions can be drawn about the overall optimality of the solution based on this approach.

An alternative to this "global" methodology is the "segment-by-segment" approach. In this case, each segment is optimized individually and sequentially. Naturally, the segment-by-segment approach is most computationally efficient in terms of speed and, as numerical evidence suggests, the overall optimality is not greatly affected. For instance, suppose the optimizer seeks to minimize the path error over the duration of the mission, that is, 180 days for the examples presented here. With a suitable initial guess, a "segment-by-segment" approach may require 20 minutes to identify the local optimal solution. The "global" approach, on the other hand, can take days to identify a solution that is only slightly better than the one identified through the "segment-by-segment" approach. Computationally, the time required to identify the optimal solution is significantly affected by the sensitivity of the dynamical regime near the libration points. That is, seemingly minuscule changes in the control inputs can lead to significant changes in the path of the deputy. In the "global" approach, this sensitivity is compounded since the method attempts to optimize all $3(N-1)$ inputs simultaneously.

In the global approach, where the terminal time is significantly larger, the dynamical sensitivity of the model forces the optimizer to seek a solution by following a sequence of extremely small steps. Since small changes have such a significant impact downstream, with each passing iteration, the steps become even smaller, further degrading the performance of the algorithm.

*Example: Minimization of State Error*

Let the path dependent term, in Equation (16), be characterized by

$$\tilde{L} = \frac{1}{2}\left(\bar{x} - \bar{x}^{\circ}\right)^T Q \left(\bar{x} - \bar{x}^{\circ}\right), \tag{35}$$

where $Q$ represents the state error weighting matrix and $\bar{x}^{\circ}$ denotes the nominal state vector of the deputy with respect to the chief spacecraft. Furthermore, let the end state term of the cost function be defined as

$$\tilde{\phi}\left(t_N\right) = \frac{1}{2}\left(\bar{y}_N - \bar{y}_N^{\circ}\right)^T W \left(\bar{y}_N - \bar{y}_N^{\circ}\right) + y_{n+1}\left(t_N\right), \tag{36}$$

where $W$ represents the end state weighting matrix and $\bar{y}_N^{\circ}$ is the nominal state of the deputy at the END of the mission. Both $Q$ and $W$ are symmetric positive definite matrices. Given these definitions, the boundary condition for the co-state vector is

$$\tilde{\lambda}_N^T = \frac{\partial \tilde{\phi}_N}{\partial \tilde{y}_N} = \left[\left(\bar{y}_N - \bar{y}_N^{\circ}\right)^T W \quad 1\right], \tag{37}$$

and the linear system matrix is given by

$$\tilde{A}\left(t\right) = \begin{bmatrix} A\left(t\right) & 0 \\ \left(\bar{y} - \bar{y}^{\circ}\right)^T Q & 0 \end{bmatrix}. \tag{38}$$

Consider a mission that requires the deputy spacecraft to maintain a complete state, relative to the chief, characterized by $\bar{r} = \left(50 \text{ m}\right)\hat{z}$ and $\dot{\bar{r}} = \bar{0}$; that is, the line formed by the chief and deputy vehicles must remain perpendicular to the ecliptic plane while, at the same time, the deputy maintains a distance of 50 m from the chief. Let the state error weighting be defined by a diagonal matrix $Q$, where $Q = diag(1\times10^{12}, 1\times10^{12}, 1\times10^{12}, 1\times10^{6}, 1\times10^{6}, 1\times10^{6})$. The time history of the radial error for various end state weightings is plotted in Figure 2. The dashed red curve represents the solution determined from a standard state corrector [17]. The blue curve is associated with the optimal control without end point weighting, $W = 0$. Note that the response in blue alternates in amplitude with respect to the standard state corrector. That is because the end state error is not constrained in this particular solution. Hence, the optimal path is allowed to overshoot the nominal as long as the overall segment error is minimized. The intermediate green curve is generated when some end point weighting is incorporated into the solution process, i.e., $W = 1\times10^{-2}Q$. If the end point weighting is increased, the optimal solution, identified as the magenta curve in Figure 2, eventually converges on the initial guess. That is, the response computed from the state differential corrector. This is not surprising since, in this case, the initial guess already satisfies the end state constraint. The red and magenta curves may be difficult to discern from this figure since they are essentially equal. However, they both incur the largest deviations relative to the nominal path.

The optimal solution curves presented in Figure 2 are associated with the segment-by-segment approach previously described. The segment-by-segment method is most computationally efficient when the trajectory is decomposed into many nodes over long periods of time. It is also possible, however, to determine the optimal maneuver scheme based on a "global" approach. In this case, all maneuvers are simultaneously optimized over the length of the mission. The efficiency of these two methods, for a 180 day mission, is contrasted in Figure 3 and Figure 4.

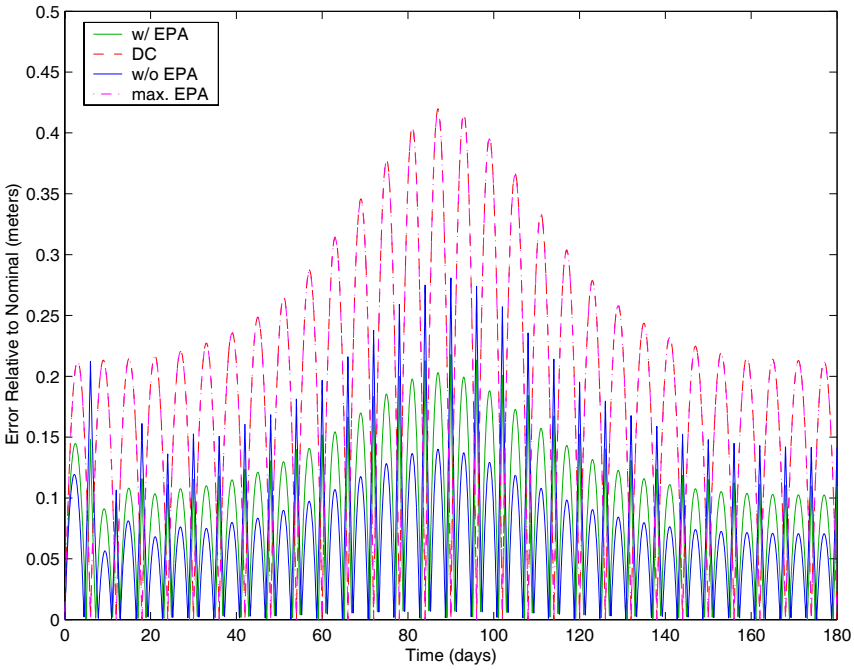


**Figure 2 - Comparison of State Corrector vs. Optimal Impulsive Control for a 50 m Formation Near an L2 Halo Orbit**

For a nominal path characterized by $\bar{r}^{\circ}(t) = 5000\hat{z}$ km, the radial error response is presented in Figure 3. The results obtained via a state differential corrector (solid blue), the segment-by-segment method (dashed green), and the global approach (solid red) are represented as three separate curves in Figure 3. The largest deviations are, of course, incurred by the solution that employs the state corrector. The remaining two curves in Figure 3 are virtually indistinguishable, except for some small differences near the peaks. Although, over certain intervals, the performance of the segment-by-segment approach appears to be slightly better than the global method, the overall value of the cost index, over 180 days, is in fact lowest for the global approach. The cost index, as a function of time, appears in Figure 4. Note that the only value of interest on this figure is the final value, $y_{n+1}(t_f)$. It is apparent, from Figure 4, that over long mission durations, the segment-by-segment approach is essentially just as effective as the global method. Although, numerically, the global approach still proves to be the true optimal solution, the differences are not significant. Either approach appears well suited in terms of reducing the overall error relative to the nominal, as deduced from Figure 3.

The most interesting and revealing information obtained from the application of these methodologies, comes from the optimal maneuver schedule in Figure 5. Three plots are presented in this figure. Let $\Delta V^{\circ}$ denote the maneuver history associated with the state corrector, used as an initial guess in solving the optimal control problem. Figure 5 depicts the difference between the optimal maneuver history and $\Delta V^{\circ}$ in mm/sec. The maneuver histories associated with both the global and the segment-by-segment methods are plotted in terms of the $x$-, $y$-, and $z$- components of the resulting $\Delta V$ time history. Given the highly sensitive nature in this dynamical regime, a formation that requires a nominal separation of 5000 km is very susceptible to small changes in the control inputs. This is particularly true as the time between maneuvers is increased. A small input results in significant change at the end of each segment. In this case, these small changes – on the order of mm/sec – reduce the overall error by almost 10 km 90 days into the mission. This particular time interval is associated with the point along the halo orbit that is closest to the $xy$-plane.

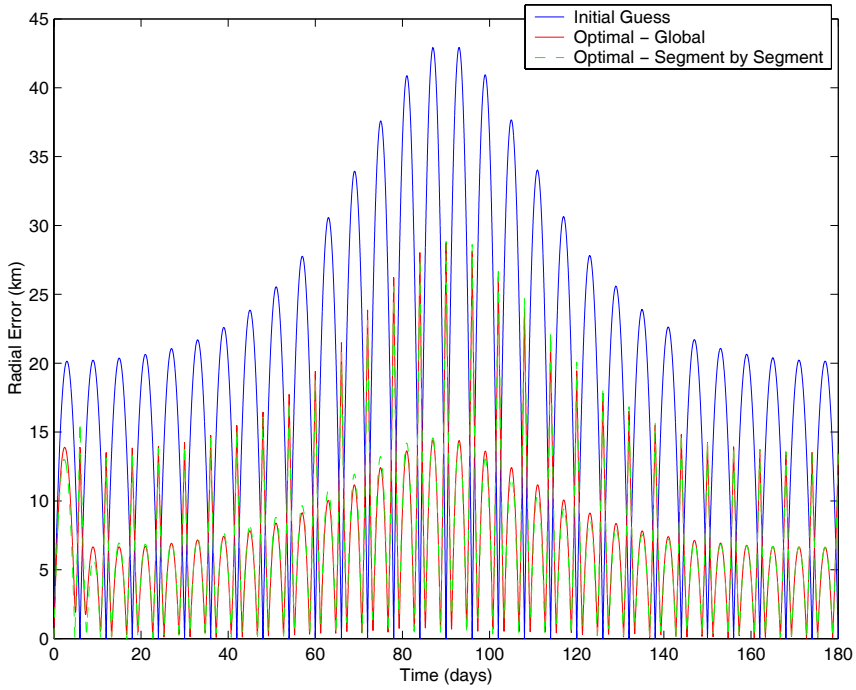


**Figure 3 - Radial Error Response – Global vs. Segment by Segment Approach Applied to a 5000 km Formation Near an L2 Halo Orbit**

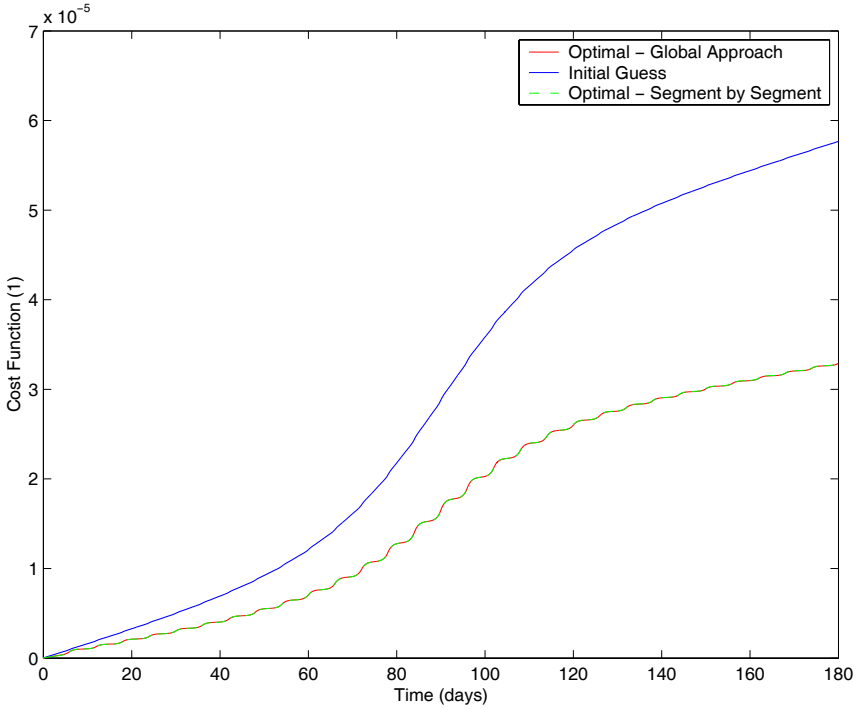


**Figure 4 - Cost Function - Global vs. Segment-by-Segment Approach Applied to a 5000 km Formation Near an L2 Halo Orbit**

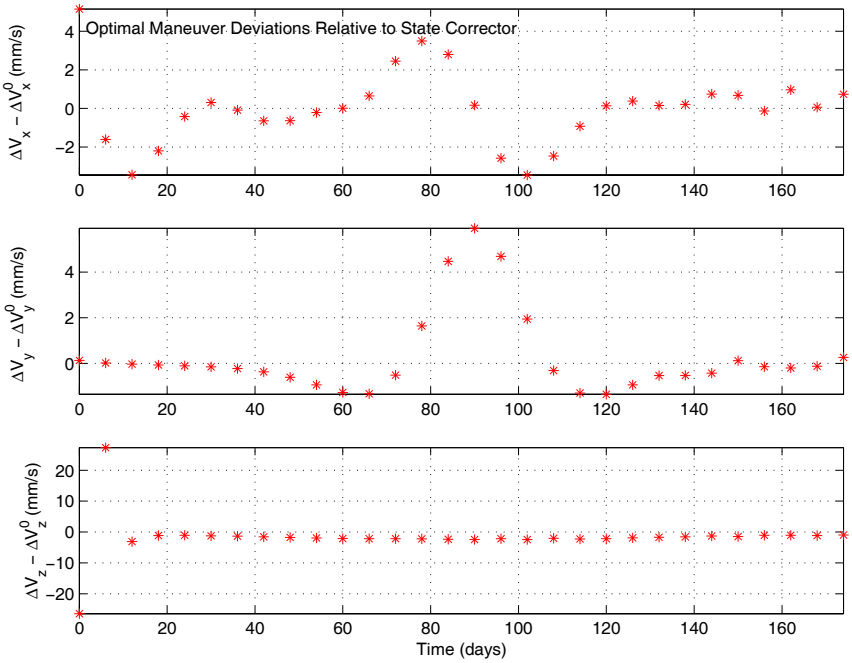


**Figure 5 - Maneuver Scheme - Global vs. Segment-by-Segment Approach Applied to a 5000 km Formation Near an L2 Halo Orbit**

It is also worth noting that, the global approach, in this case, is computationally intensive and requires more than one day of processing time to generate a solution. The segment-by-segment approach, on the other hand, is successful within minutes. Since the results from the two methodologies are comparable it appears that the segment-by-segment method represents a reasonable alternative to the global approach.

*Example: Minimize Range Error*

Missions like MAXIM and TPF require that the deputies in the formation track some pre-specified nominal path within a specified level of accuracy. However, for other missions, it may be sufficient to maintain the deputy at a constant relative distance from the chief vehicle. The radial targeter presented in this chapter proves to be most effective in accomplishing such a task. In contrast to the state corrector, the deviations from the specified nominal radial distance are minimal in comparison to the deviations incurred by the state targeter. The solution obtained from the radial targeter can also serve as an initial guess to the optimal impulsive control scheme described here. In this case, the cost function can be expressed as

$$\tilde{L} = \frac{1}{2} q \left( r - r^{\circ} \right)^2. \tag{39}$$

The goal of the optimal control law, associated with the above definition, is to minimize the range error between the deputy and chief vehicles over the duration of the mission. Note that the weighing factor $q$ is actually necessary – for the examples considered here – because the initial guess, from the radial corrector [16], is very close to the optimal solution, as is apparent in Figure 6. In this figure, the radial distance between the chief and deputy vehicle is plotted over a period of 180 days. Three curves are depicted. The dash-dot red curve represents the initial guess for the optimizer. The dashed green curve is the optimal solution associated with the "segment-by-segment" approach. Finally, the solid blue line represents the optimal solution determined from the "global" approach.

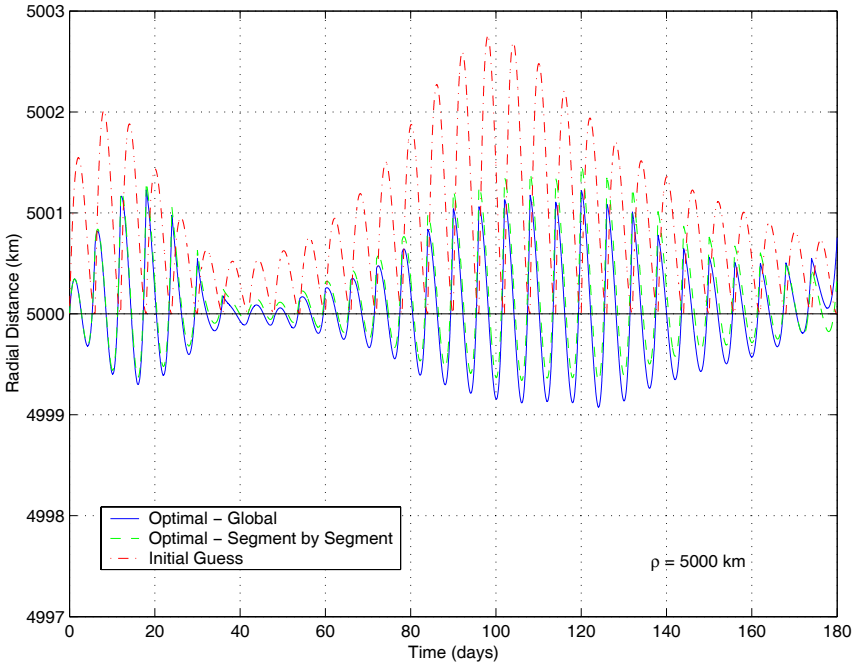


**Figure 6 - "Global" Optimal Solution for Radial Tracking**

Although there is visible improvement between the initial guess and the optimal solutions, it is not as significant as that determined in the previous section for state tracking example. Recall that, in the previous example, a 5000 km formation incurred an error of up to 40 km between maneuvers via the corrector scheme. In the present example, the radial corrector leads to errors under 3 km for a nominal 5000 km separation. In tracking the radial distance, although the "segment-by-segment" and "global" methods lead to similar solutions, the "global" approach leads to the true optimal, as deduced from Figure 7. In this figure, the final value of the cost function represents the quantity that is actually optimized, $x_{n+1}(t_N)$.

It is evident, from Figure 7, that the "optimal" exhibits only marginal improvement over the solution determined with the radial corrector. The optimal maneuver history associated with the path in Figure 6 is plotted in Figure 8. Although the difference between the maneuvers determined with the radial corrector and the optimal control law are visible, as further demonstrated in Figure 9, the two optimal approaches converged onto similar solutions. Figure 10 highlights the difference between the control inputs as determined from the "segment-by-segment" and "global" methods. These differences are only on the order of $10^{-6}$ m/sec and, yet, such small inputs are enough to generate a visible difference in the optimal solution, as observed in Figure 6. The differences in the optimal path are most visible near the end of the mission; another indication of the dynamical sensitivity of the model.

Recall that the goal of the radial corrector is to minimize the range error at the end of each segment rather than over the duration of the mission. Since the optimal solution is so close to the initial guess, in this case, if no weighting $q$ is present the numerical process will assume that the optimal has been achieved without ever actually computing an optimal control effort. The weighting depends on the nominal relative separation between the vehicles. For instance, for a 5000 km nominal radial distance, a weighting – in the non-dimensional equations – of $1\times10^{8}$ is appropriate. However, for a 50 m formation a weighting on the order of $1\times10^{12}$ is most suitable. This further validates the observation that an alternate scaling of the state variables may, at times, prove beneficial in reducing the time required to identify an optimal solution. Such re-scaling may also allow for larger tolerances during the optimization process. This observation is confirmed during the second approach involving nonlinear programming.

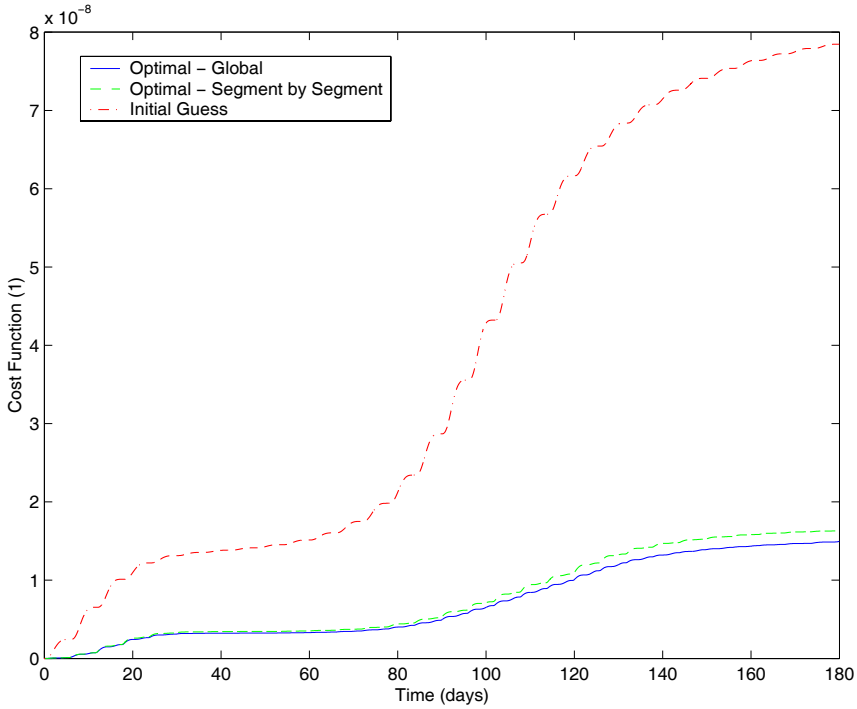


**Figure 7 - Cost Functional (Non-Dimensional) for Radial Tracking Example**

Method #2: Optimal Control by Transcription

As previously mentioned, the nonlinear optimality conditions employed in the present development are based on the calculus of variations. As such, the startup solution for the optimization process is assumed to exist in the vicinity of the optimal trajectory. For instance, if the goal of the optimization process is to establish a non-natural yet periodic relative orbit, then the initial guess must be nearly periodic. In this study, a Floquet approach [17] is first implemented to numerically identify a suitable startup solution. This trajectory arc is later transitioned into the nonlinear system via the two-level differential corrections process developed by Howell and Pernicka [27]. Naturally, periodic relative orbits do not exist in the general *n*-body problem. However, nearly periodic or slowly drifting relative arcs do exist naturally in this regime. For the present example, these trajectory arcs represent excellent startup solutions for the optimization process.

*Problem Formulation*

An optimal control problem can be formulated as a collection of $N$ phases. Thus, if time is the independent variable for each phase, then $t_i^{(k)} \le t \le t_f^{(k)}$. Here, the subscripts $i$ and $f$ identify the initial and terminal states along the phase. Within a given phase, the dynamics of the system are described by a set of dynamic variables,

$$\bar{z}^{(k)} = \begin{bmatrix} \bar{y}^{(k)}(t) \\ \bar{u}^{(k)}(t) \end{bmatrix}, \tag{40}$$

made up of $n^{(k)}$ state variables and $n_u{}^{(k)}$ control variables, respectively. In addition, the dynamics may also incorporate a vector of time invariant parameters, $\bar{p}^{(k)}$, of dimension $n_p{}^{(k)}$. For notational simplicity, the superscript $(k)$ is discontinued from this point on. However, it is important to remember that many complex problems require different dynamical models and/or constraints within each phase, and the approach accommodates this requirement.

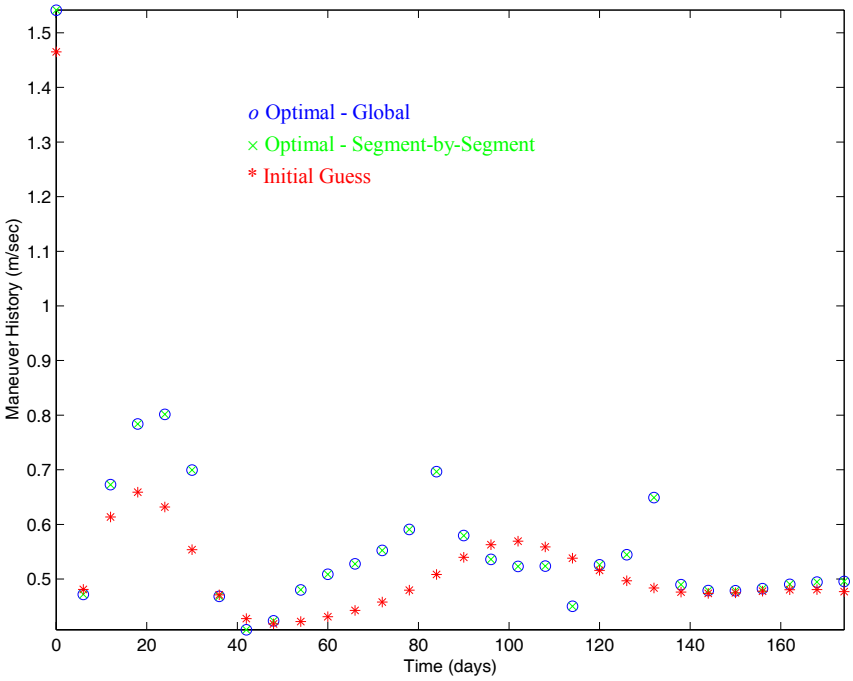


**Figure 8 - Maneuver History for Radial Tracking Example**

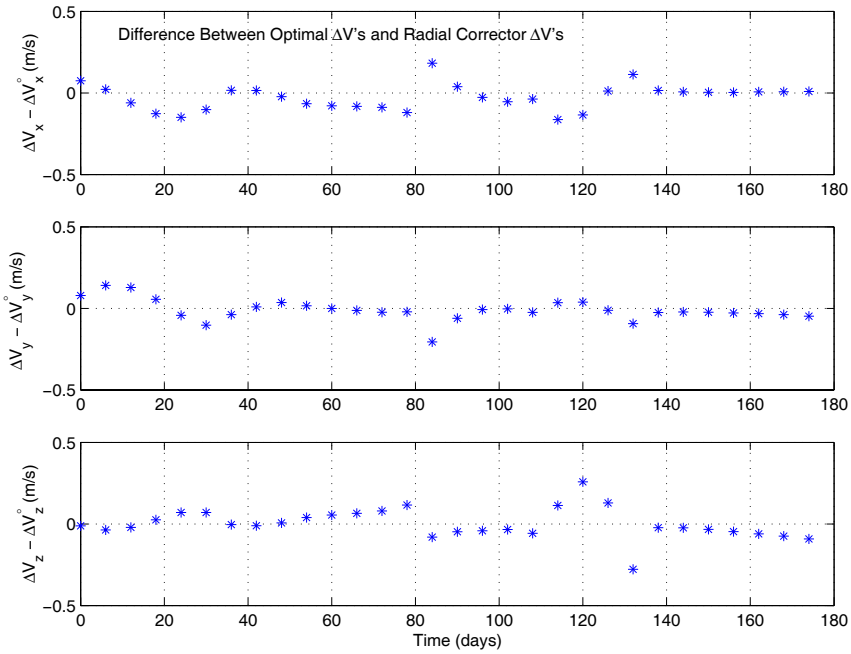


**Figure 9 - Maneuver Comparison to Radial Corrector ( $\Delta\bar{V}^{\circ}$ ) Results**

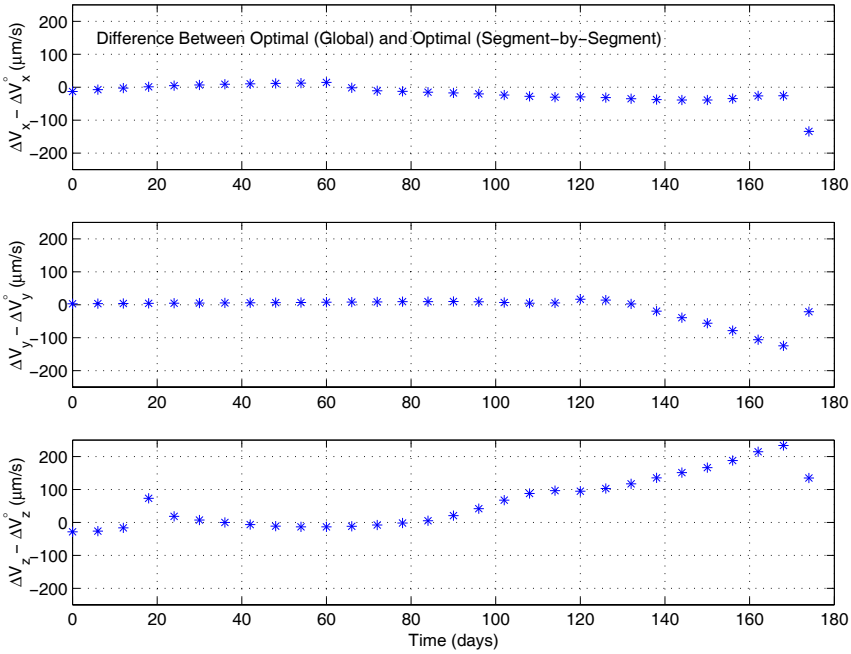


**Figure 10 - Optimal Maneuver Comparison**

In general, the optimal control problem requires the identification of an $n_u$ - dimensional control vector, $\bar{u}(t)$, that minimizes the performance index $J = \phi\left(\bar{y}(t_f), t_f\right)$ evaluated at the final time $t_f$. The dynamics of the system are defined by the state equations

$$\dot{\bar{y}} = \bar{f}\left(\bar{y}(t), \bar{u}(t), \bar{p}, t\right). \tag{41}$$

Initial conditions, at time $t_i$, are defined by

$$\bar{\psi}_{i_l} \le \bar{\psi}_i\left[\bar{y}(t_i), \bar{u}(t_i), t_i\right] \le \bar{\psi}_{i_u} \tag{42}$$

and terminal conditions at the final time $t_f$ are defined by

$$\bar{\psi}_{f_l} \le \bar{\psi}_f\left[\bar{y}(t_f), \bar{u}(t_f), t_f\right] \le \bar{\psi}_{f_u} \tag{43}$$

In addition, the solution must satisfy algebraic path constraints of the form

$$\bar{g}_l \le \bar{g}\left[\bar{y}(t), \bar{u}(t), t\right] \le \bar{g}_u \tag{44}$$

where $\bar{g}$ is a vector of size $n_g$. The optimization process is significantly aided by defining a search area. This is accomplished by specifying bounds on the state variables,

$$\bar{y}_l \le \bar{y}(t) \le \bar{y}_u, \tag{45}$$

the control variables

$$\bar{u}_l \le \bar{u}(t) \le \bar{u}_u, \tag{46}$$

and the time invariant parameters,

$$\bar{p}_l \le \bar{p} \le \bar{p}_u. \tag{47}$$

Note that, for Equations (42) through (47), an equality constraint can always be imposed simply by equating the upper and lower limits of the specified range.

The basic optimal control problem is to determine the $n_u^{(k)}$-dimensional control vectors, $\bar{u}^{(k)}(t)$ and parameters $\bar{p}^{(k)}$ to minimize the performance index,

$$J = \phi\left[\bar{y}\left(t_i^{(1)}\right), t_i^{(1)}, \bar{y}\left(t_f^{(1)}\right), t_f^{(1)}, \bar{p}^{(1)}, \ldots, \bar{y}\left(t_i^{N}\right), t_i^{N}, \bar{y}\left(t_f^{(N)}\right), t_f^{(N)}, \bar{p}^{(N)}\right] + \sum_{k=1}^{N} \int_{t_i^{(k)}}^{t_f^{(k)}} q^{(k)}\left[\bar{y}^{(k)}(t), \bar{u}^{(k)}(t), \bar{p}^{(k)}, t\right] dt \quad . \tag{48}$$

Notice that, in the above formulation, the cost function may depend on quantities computed in each of the $N$ phases.

*Transcription Formulation*

The basic approach for solving the optimal control problem by transcription is discussed by Betts [20]. In a transcription approach, the time interval of every phase is divided into $n_s$ segments

$$t_i < t_1 < t_2 < \ldots < t_f = t_{n_s} . \tag{49}$$

The associated states along the trajectory are then defined as mesh points, grid points, or nodes. Let us introduce the notation $\bar{y}_j = \bar{y}\left(t_j\right)$ to indicate the value of the state variable at a grid point. In like fashion denote the control at this grid point by $\bar{u}_j = \bar{u}\left(t_j\right)$. In a direct transcription method, the nonlinear system in Equation (41) is represented by a system of defect equality constraints that are enforced at each grid point. For example, in a compressed Hermite-Simpson discretization, the NLP variables for any given phase are

$$\bar{x} = \left[\bar{y}_i, \bar{u}_i, \bar{u}_i', \bar{y}_1, \bar{u}_1, \bar{u}_1', \ldots, \bar{y}_f, \bar{u}_f, \bar{p}, t_i, t_f\right] . \tag{50}$$

At each node, then, the state equations are approximately satisfied by setting the defects

$$\bar{\zeta}_j = \bar{y}_j - \bar{y}_{j-1} - \frac{h_j}{6}\left[\bar{f}_j + 4\bar{f}_j' + \bar{f}_{j-1}\right], \tag{51}$$

where

$$\bar{f}_j' = \bar{f}\left[\bar{y}_j', \bar{u}_j', \bar{p}, t'\right], \tag{52}$$

with

$$\bar{y}_j' = \frac{1}{2}\left[\bar{y}_{j-1} + \bar{y}_j\right] + \frac{h_j}{8}\left[\bar{f}_{j-1} - \bar{f}_j\right], \tag{53}$$

for $j = 1, \ldots, n_s$. The step size is denoted by $h_j = t_j - t_{j-1}$, and the right hand side of the differential equations, evaluated at grid point $j$, is denoted by the vector $\bar{f}_j$. The state and control variable bounds, in Equations (45) and (46), become simple bounds on the nonlinear programming (NLP) variables. The defect constraints and variable bounds are imposed at <u>all</u> the grid points, including the midpoints $\bar{y}_j'$. As a result of the transcription process the differential-algebraic system defining the optimal control problem, for each phase, is replaced by the NLP constraints

$$\bar{c}_l \le \bar{c}\left(\bar{x}\right) \le \bar{c}_u , \tag{54}$$

where

$$\bar{c}\left(\bar{x}\right) = \left[\zeta_1, \zeta_1', \zeta_2, \zeta_2', \ldots, \zeta_f, \bar{\psi}_i, \bar{\psi}_f, \bar{g}_i, \bar{g}_1, \ldots, \bar{g}_f\right], \tag{55}$$

with

$$\bar{c}_l = \left[0, \ldots, 0, \bar{\psi}_{i_l}, \bar{\psi}_{f_l}, \bar{g}_{i_l}, \ldots, \bar{g}_{f_l}\right], \tag{56}$$

and a corresponding definition of $\bar{c}_u$.

The first set of equality constraints above require that the defect vectors from each of the $n_s$ segments be zero, thereby approximately satisfying the differential equations. The boundary conditions denoted by $\bar{\psi}_l$ and $\bar{\psi}_f$ are enforced directly as equality constraints, and nonlinear path constraints denoted by $\bar{g}$ are imposed at the grid points along the corresponding phase. Note that nonlinear equality path constraints are accommodated by setting $\bar{g}_l = \bar{g}_u$. Similarly, the state and control variable bounds become simple bounds on the NLP variables. This large, sparse, NLP can be solved efficiently using either a sequential quadratic programming (SQP) method or an interior point (barrier) method.

In summary, three primary operations are performed in solving an optimal control problem by transcription:

1. Direct Transcription → Transcribe the optimal control problem into a nonlinear programming (NLP) problem by discretization.

2. Sparse Nonlinear Program → Solve the sparse NLP using either sequential quadratic programming (SQP) or an interior point (barrier) method.

3. Mesh refinement → Assess the accuracy of the approximation (i.e., the finite dimensional problem) and, if necessary, refine the discretization and repeat the optimization steps.

*Solution of the Nonlinear Program*

As previously mentioned, the Sparse Optimal Control Software (SOCS), developed by Betts, is employed here to solve the optimal control problem. Within SOCS, a sequential quadratic programming (SQP) approach is used to solve the nonlinear programming problem that results from transcription of the optimal control problem. In this case, the cost function may be expressed as

$$J = F(\bar{x}), \tag{57}$$

subject to

$$\bar{c}_l \le \bar{c} \le \bar{c}_u, \tag{58}$$

and

$$\bar{x}_l \le \bar{x} \le \bar{x}_u. \tag{59}$$

The constraints in Equations (58) and (59) may then be introduced into the cost function by introducing Lagrange multipliers $\bar{\lambda}$ and $\bar{v}$,

$$L(\bar{x}) = F(\bar{x}) - \bar{\lambda}^T \bar{c}(\bar{x}) - \bar{v}^T \bar{x}. \tag{60}$$

In a quadratic programming (QP) approach, the Lagrangian in Equation (60) is approximated to second order via a Taylor series expansion,

$$L(\bar{x}) \approx \left.\frac{\partial L}{\partial \bar{x}}\right|^* (\bar{x} - \bar{x}^*) + \frac{1}{2}(\bar{x} - \bar{x}^*)^T \left[\left.\frac{\partial}{\partial \bar{x}}\left(\frac{\partial L}{\partial \bar{x}}\right)\right|^*\right](\bar{x} - \bar{x}^*) = \bar{\gamma}^T \bar{s} + \frac{1}{2}\bar{s}^T H \bar{s}, \tag{61}$$

where $\bar{x}^*$ represents the reference solution.

The vector $\bar{x} - \bar{x}^*$ is defined as the search direction, $\bar{s}$, and is identified by minimizing the quadratic in Equation (61) subject to the linear constraints

$$\bar{b}_l \le \begin{bmatrix} \Gamma\bar{s} \\ \bar{s} \end{bmatrix} \le \bar{b}_u, \tag{62}$$

where $\bar{\gamma} = \nabla_{\bar{x}} \bar{f}(\bar{x})$ is the $N$-dimensional gradient vector, $\Gamma$ is the $m \times N$ Jacobian matrix of constraint gradients, and $H$ is a symmetric $N \times N$ positive definite approximation to the Hessian matrix. The upper bound vector is defined by

$$\bar{b}_u = \begin{bmatrix} \bar{c}_u - \bar{c} \\ \bar{x}_u - \bar{x} \end{bmatrix}, \tag{63}$$

with a similar definition for the lower bound vector $\bar{b}_l$. In SOCS, the gradient and Hessian information required by the optimization algorithm are computed through sparse finite differencing, as discussed by Betts [24]. The sparse quadratic program is then solved using a Schur-Complement Method proposed by Gill, Murray, Saunders, and Wright [28].

*Example: Closed Relative Path via Impulsive Control*

Suppose that the optimal control problem is defined as the minimization of the cost index,

$$J = \Delta\bar{V}(t_0)^T \Delta\bar{V}(t_0), \tag{64}$$

where $\Delta\bar{V}(t_0)$ denotes a single impulsive maneuver applied at the initial state along the trajectory. This maneuver is required to achieve a closed relative path in position. Subsequently, the cost index in Equation (64) is subject to a position vector path constraint,

$$\bar{r}(t_f) - \bar{r}(t_0) = 0, \tag{65}$$

where, for any $j$, $\bar{r}(t_j)$ represents the relative position vector that locates the deputy vehicle with respect to the chief spacecraft at time $t_j$. Thus, $t_0$ and $t_f$ denote the initial and final times, respectively. This constraint is in addition to the dynamical constraint defined by the equations of motion,

$$\dot{\bar{y}} = \bar{f}(\bar{y}(t)). \tag{66}$$

Furthermore, the trajectory arc is subject to an initial condition

$$\bar{y}(t_0) = \begin{bmatrix} \bar{r}(t_0) \\ \bar{V}^-(t_0) \end{bmatrix} = \bar{y}_0, \tag{67}$$

and an initial velocity constraint,

$$\bar{V}^+(t_0) - \bar{V}^-(t_0) - \Delta\bar{V}(t_0) = 0. \tag{68}$$

In Equation (68), $\bar{V}^-(t_0)$ represents the pre-defined velocity at the start of the trajectory segment and $\bar{V}^+(t_0)$ the velocity after the corrective $\Delta\bar{V}$ is applied. Figure 11 illustrates one sample trajectory obtained from this optimization process. In this particular example, the reference halo orbit is characterized by a maximum out-of-plane excursion of 300,000 km. The path illustrated in Figure 11, then, represents the trajectory of the deputy vehicle relative to the chief, located at the origin of each plot. In this particular example, forcing a closed path only requires a maneuver on the order of $10^{-6}$ m/sec.

Note, relative orbits ranging in size from 10 meters to 100,000 km were considered during this investigation. Although the methodology is unaffected by the startup solution, some of the parameters employed can significantly impact the success of the numerical solution process. Numerical evidence suggests this process benefits from reducing the order of the system of equations.

For example, in past investigations [13-17], the path of the chief spacecraft and deputy vehicles are simultaneously integrated. However, in the present study, the transcription process introduces some difficulties related to relative variable scaling. Some of these difficulties may be overcome if the chief spacecraft path is determined first and the results are subsequently represented using B-spline coefficients. Then, to evaluate the right hand side of the deputy equations of motion, the chief spacecraft coordinates are determined by evaluating these coefficients at the requested times. Thus, the optimizer is applied to 6 equations of motion instead of 12.

Other scaling difficulties arise if the non-dimensional form of the equations of motion is employed. For example, traditionally, the characteristic length and time are defined as the mean distance between the Earth and the Sun and the inverse of the Earth's mean motion, respectively. Since the nominal formations presently under consideration do not exceed distances over 20,000 km from the chief spacecraft, the resulting position, velocity, and control acceleration variables are disproportionately scaled. Thus, it is often necessary to place some weighting on the position, velocity, and control accelerations to alleviate the convergence difficulties introduced by the scaling differences.

*Example: Periodic Relative Path via Continuous Control*

In the above example, the startup solution is sufficiently close to periodic that the resulting optimal solution appears, at least, to be both closed and smooth. However, nearly vertical relative trajectories, identified by Howell and Marchand [17], do not lend themselves to this type of solution. Although it is possible to identify an optimal impulsive maneuver that leads to a closed arc, the velocity discontinuity at the end of the segment is typically significant and leads to a non-smooth solution. To remedy this difficulty, the problem is posed as one of continuous optimal control instead.

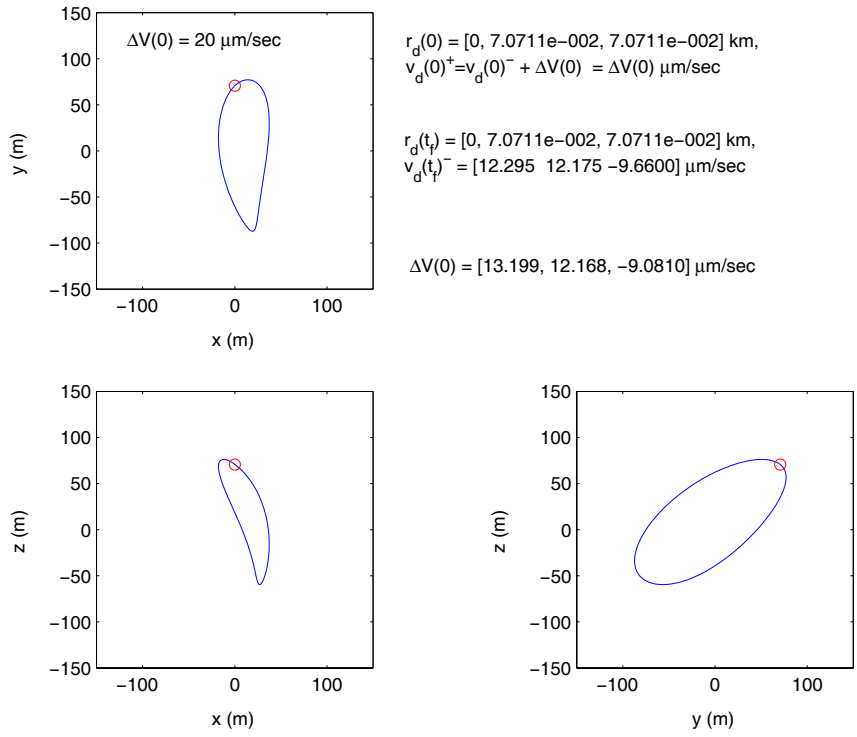


**Figure 11 – Periodic Relative Orbits via Impulsive Optimal Control**

Once again, SOCS is used to solve the optimal control problem. In this case, the goal is to identify the control history, $\bar{u}(t)$, that minimizes

$$J = \sum_{k=1}^{N} \int_{t_i^{(k)}}^{t_f^{(k)}} \bar{u}^T(t)\bar{u}(t)dt, \tag{69}$$

subject to the equations of motion in Equation (66) and the initial conditions in Equation (67). The initial state is associated with a fixed initial time, $t_i$, while $t_f$ is defined as the final time required to achieve $\bar{y}(t_i) = \bar{y}(t_f)$. In this particular example, the startup relative orbit has a maximum *z*-component, as defined in the synodic rotating frame, of 1000 km. Given the sensitivity of the dynamical system to small perturbations, the solution is divided into four phases to facilitate the solution process. Thus, the following constraints are imposed on the cost index,

$$t_i^{(k)} = \text{fixed, for } k = 1,\ldots,4, \tag{70}$$

$$t_f^{(k)} = \text{fixed, for } k = 1,\ldots,4, \tag{71}$$

$$\bar{r}\left(t_i^{(1)}\right) - \bar{r}_i = 0, \tag{72}$$

$$\bar{u}\left(t_i^{(1)}\right) = 0, \tag{73}$$

$$\bar{z}\left(t_f^{(k)}\right) - \bar{z}\left(t_i^{(k+1)}\right) = 0, \quad k = 1,\ldots,3, \tag{74}$$

$$\bar{y}\left(t_i^{(1)}\right) - \bar{y}\left(t_f^{(4)}\right) = 0. \tag{75}$$

Equations (70)-(71) simply specify that the initial and terminal times of each phase are fixed. These are included in the optimization process as part of the parameter vector, $\bar{p}^{(k)}$ for a given phase. The constraints in Equations (72)-(73) specify that the initial position along the startup solution is fixed as is the initial control effort, assumed to be zero. Note that the initial guess for the control vector at each node is actually set to zero since the startup solution represents a naturally existing arc that is already close to the desired path. Equation (74) ensures continuity in both the state vector and the control accelerations across phases. Finally, the periodicity constraint is introduced in Equation (75).

An optimal solution is sought in the vicinity of the startup solution. Thus, it is appropriate to specify bounds on the states and control variables to assist the convergence of the numerical process. In this case, the following bounds are arbitrarily selected,

$$\begin{bmatrix} -10{,}000 \text{ km} \\ -10{,}000 \text{ km} \\ -10{,}000 \text{ km} \\ -4 \text{ m/sec} \\ -4 \text{ m/sec} \\ -4 \text{ m/sec} \end{bmatrix} \le \bar{y}(t) \le \begin{bmatrix} 10{,}000 \text{ km} \\ 10{,}000 \text{ km} \\ 10{,}000 \text{ km} \\ 4 \text{ m/sec} \\ 4 \text{ m/sec} \\ 4 \text{ m/sec} \end{bmatrix}, \tag{76}$$

and

$$\begin{bmatrix} -4 \text{ m/s}^2 \\ -4 \text{ m/s}^2 \\ -4 \text{ m/s}^2 \end{bmatrix} \le \bar{u}(t) \le \begin{bmatrix} 4 \text{ m/s}^2 \\ 4 \text{ m/s}^2 \\ 4 \text{ m/s}^2 \end{bmatrix}. \tag{77}$$

Once again, the chief spacecraft path is assumed to be pre-determined and is represented using B-spline coefficients. Furthermore, based on previous observations regarding the non-dimensional form of the equations of motion (EOMs), a dimensional set of EOMs is employed instead. However, the previous example involved a single impulsive maneuver. Here, the control problem involves continuous thrusting over 180 days. Thus, the thrust levels are extremely low further complicating the numerical solution

process.

These low thrust levels pose a challenge due to the accuracy of the transcription process and the internal tolerance limits in SOCS. To circumvent these limitations, the dimensional equations of motion (km, km/sec), are also subject to some internal re-scaling. In this case, the position elements are scaled down by $10^{-3}$, while the velocities and control accelerations are scaled up by $10^{3}$ and $10^{6}$, respectively. Whether or not internal re-scaling is necessary can only be determined, of course, on a case by case basis and is a matter of engineering judgment.

The results of the optimization process are illustrated in Figure 12. The trajectory in Figure 12 represents the path that a deputy spacecraft follows as the chief vehicle evolves along a halo orbit. The origin of this figure represents the chief spacecraft itself. In the present example, the chief spacecraft is assumed to follow a periodic halo orbit, as determined in the CR3BP, characterized by a maximum out-of-plane amplitude of 300,000 km. Thus, the deputy path observed in Figure 12 is associated with the CR3BP. The open red arc identifies the startup solution. The closed blue arc, then, represents the converged optimal solution via continuous control. The associated control accelerations are illustrated in Figure 13. Note that the control effort is highest near the start and end of the trajectory, where the periodicity constraint is enforced. Otherwise, the trajectory in Figure 12 is very close to the startup solution and, as such, the control accelerations near the lower $z$-amplitudes are smallest near this region.

Note that the problem is carefully formulated to ensure a smooth transition into the ephemeris model. Basically, the transition only requires a change on the right hand side of Equation (66). As previously mentioned, the chief spacecraft path is pre-determined outside of the optimization process and later approximated using splines. This particular approach is consistent with past developments involving continuous control and formation flight near the libration points as determined in the ephemeris model [14]-[17]. Of course, for formation flight in the ephemeris model, the spline coefficients are associated with a quasi-periodic Lissajous trajectory, rather than a periodic halo orbit. Furthermore, in the ephemeris model, the relative equations of motion are formulated in the inertial frame associated with the JPL DE405 ephemeris, instead of the synodic rotating frame of the CR3BP.

This particular example represents a step towards a greater goal, that is, to incorporate constrained nonlinear optimal control in the ephemeris model through the use of existing and proven software tools. The ultimate success of these examples brings about the solution to multiple issues related to the numerical sensitivities of the problem. Naturally, in working with any existing optimization software packages, it is important to keep in mind the traditional applications and the internal limitations of the software. For formation keeping near the libration points, the differences in scale between the position elements, the relative velocities, and the necessary control accelerations is quite significant. Oftentimes, the control effort necessary to achieve a prescribed nominal motion can be extremely small yet crucial in achieving the desired nominal accuracy.

In the two examples presented here, involving impulsive and continuous control, addressing the variable scales problem is critical in the success of the optimization process. Because of these scale differences, it is not surprising to find that the traditional non-dimensional formulation of the dynamical model is inadequate based on the numerical methods employed and the associated limitations in accuracy. Past investigations [13-16] consider continuous control in both the CR3BP and the ephemeris model using high accuracy integrators to identify the desired solutions. Clearly, a numerical integration approach leads to solutions that are continuous and smooth in all variables. In a nonlinear programming approach, however, continuity is, in fact, a constraint that may not always be achieved to within the expected tolerance levels. In fact, what seems like a reasonable tolerance, in the non-dimensional system, may lead to unacceptable discontinuities in the solution.

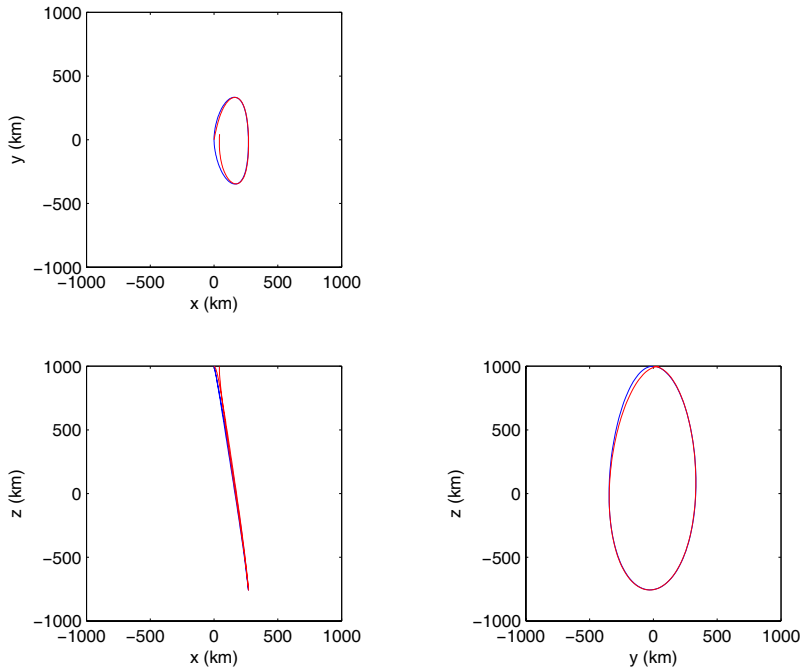


**Figure 12 - Periodic Relative Orbit via Continuous Optimal Control**

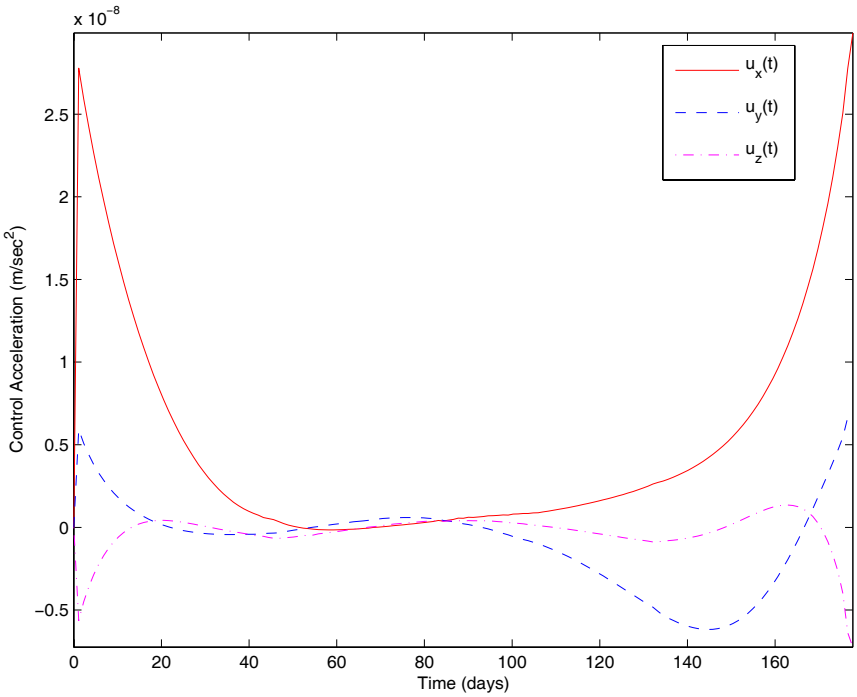


**Figure 13 - Continuous Optimal Control Acceleration History**

To illustrate this, consider that an acceleration on the order of $10^{-9}$ m/sec$^2$ translates into a non-dimensional control input on the order of $10^{-7}$ non-dimensional units. If the internal tolerances of the software do not allow for tolerances below this level, then it is possible for the optimizer to converge onto a discontinuous control time history, even if the solution appears continuous in position and velocity. Naturally, discontinuities in the control input make the remaining results suspect. For instance, changing some of the internal scaling of the optimization process can lead to essentially identical results in position and velocity while the control acceleration histories appear totally different simply because these were small enough to fall below the tolerances allowed by the software. In essence, the optimizer is fooled into believing the present solution meets all the constraints. In this case, a simple internal rescaling of the states and control inputs is insufficient. However, the combination of the dimensional equations with the internal rescaling can be quite successful in achieving continuity on all variables.

## CONCLUSIONS

The focus of this investigation is on formation keeping near the libration points via nonlinear optimal control. This is an initial step towards implementing, in a more practical capacity, constrained nonlinear optimal control in the ephemeris model. The examples presented here include optimal impulsive and continuous control. Two methodologies are considered in solving the optimal control problem. In either approach, a discrete representation of the equations of motion is necessary. Both methods divide the trajectory into segments consisting of grid points or nodes. The first method employs numerical integration to determine both the state at each node as well as the gradients needed for the optimization process. The second method does not use numerical integration directly. Instead, the states at each node are approximated from defect equations based on a Hermite-Simpson discretization. Then, the problem is reduced to one of nonlinear programming. The resulting state equations, the boundary conditions, and the path constraints are all grouped into a large sparse system of constraint equations. The solution to the optimal control problem is obtained via sequential quadratic programming by approximating the cost index to second order, subject to the augmented system of constraints, and numerically estimating the Jacobian and Hessian matrices using sparse finite differencing.

The first method, based on a subspace trust region method, employs a discretization scheme that offers greater accuracy while sacrificing performance. The second method sacrifices some accuracy in the interest of computational efficiency. This particular approach incorporates the Sparse Optimal Control Software (SOCS), developed by Betts [20], into the formation keeping analysis. The analysis reveals some numerical difficulties associated with the initial formulation of the dynamical model and the numerical methods employed in SOCS. However, these issues are overcome by introducing an alternate form for the dynamical model along with some internal rescaling of variables. The success of the examples presented here lay the foundation for future efforts to incorporate nonlinear programming in the solution of the constrained optimal formation keeping problem.

## ACKNOWLEDGEMENTS

Any opinions, findings, and conclusions or recommendations expressed in this material are those of the authors and do not necessarily reflect the views of the National Aeronautics and Space Administration.

This research was carried out at Purdue University. Support for this work was provided by Purdue University and NASA under Cooperative Agreement NCC5-727 through the NASA GSFC Formation Flying NASA Research Announcement and through Grant Number NNG04GP69G.

**REFERENCES**

1. Scheeres, D. J., and Vinh, N. X., 2000, Dynamics and control of relative motion in an unstable orbit. AIAA/AAS Astrodynamics Specialist Conference, 14-17 August 2000 (Denver, Colorado: AIAA). AIAA Paper 2000-4135.

2. Gurfil, P., and Kasdin, N. J., 2001, Dynamics and control of spacecraft formation flying in three-body trajectories, AIAA Guidance, Navigation, and Control Conference and Exhibit, 6-9 August 2001 (Montreal, Canada: AIAA). AIAA Paper 2001-4026.

3. Gurfil, P., Idan, M., and Kasdin, N. J., 2002, Adaptive neural control of deep-space formation flying. American Control Conference, 8-10 May 2002 (Anchorage, Alaska: ACC), pp. 2842-2847.

4. Hamilton, N. H., 2001, Formation flying satellite control around the L2 Sun-Earth libration point. M.S. Thesis, George Washington University, Washington, DC, December 2001.

5. Folta, D., Carpenter, J. R., and Wagner, C., 2000, Formation flying with decentralized control in libration point orbits. International Symposium: Spaceflight Dynamics, June 2000 (Biarritz, France).

6. Barden, B. T., and Howell, K. C., 1998, Fundamental motions near collinear libration points and their transitions. *The Journal of the Astronautical Sciences*, **46**(4), 361-378.

7. Barden, B. T., and Howell, K. C., 1998, Formation flying in the vicinity of libration point orbits. *Advances in Astronautical Sciences*, **99**(2), 969-988.

8. Barden, B. T., and Howell, K. C., 1999, Dynamical issues associated with relative configurations of multiple spacecraft near the Sun-Earth/Moon L1 point. AAS/AIAA Astrodynamics Specialists Conference, 16-19 August 1999 (Girdwood, Alaska: AAS), AAS Paper 99-450.

9. Howell, K. C., and Barden, B. T., 1999, Trajectory design and stationkeeping for multiple spacecraft in formation near the Sun-Earth L1 point. IAF 50th International Astronautical Congress, 4-8 October 1999 (Amsterdam, Netherlands: IAF/IAA). IAF/IAA Paper 99-A707.

10. Gómez, G., Lo, M., Masdemont, J., and Museth, K., 2001, Simulation of formation flight near Lagrange points for the TPF mission. AAS/AIAA Astrodynamics Conference, 30 July - August 2 2001 (Quebec, Canada: AAS). AAS Paper 01-305.

11. Howell, K. C., and Keeter, T., 1995, Station-keeping strategies for libration point orbits - target point and Floquet mode approaches. *Advances in the Astronautical Sciences,* **89**(2), 1377-1396.

12. Gómez, G., Howell, K. C., Masdemont, J., and Simó, C., 1998, Station-keeping strategies for translunar libration point orbits. *Advances in Astronautical Sciences*, **99**(2), 949-967.

13. Howell, K. C., and Marchand, B. G., 2003, Control strategies for formation flight in the vicinity of the libration points. AAS/AIAA Space Flight Mechanics Conference, 9-13 February 2003 (Ponce, Puerto Rico: AAS), AAS Paper 03-113.

14. Marchand, B. G., and Howell, K. C., 2003, Formation flight near L1 and L2 in the Sun-Earth/Moon ephemeris system including solar radiation pressure. AAS/AIAA Astrodynamics Specialists Conference, 3-8 August 2003 (Big Sky, Montana: AAS). AAS Paper 03-596.

15. K.C. Howell and B.G. Marchand, Design and Control of Formations Near the Libration Points of the Sun-Earth/Moon Ephemeris System. In Proceedings of the Space Flight Mechanics Symposium – Goddard Space Flight Center, Greenbelt, Maryland, October 2003.

16. K.C. Howell and B.G. Marchand. Formations Near the Libration Points: Design Strategies Using Natural and Non-Natural Arcs. In Proceedings of the GSFC 2nd International Symposium on Formation Flying Missions and Technologies, Greenbelt, Maryland, September 2004.

17. K.C. Howell and B.G. Marchand, Natural and Non-Natural Spacecraft Formations Near the L1 and L2 Libration Points in the Sun-Earth/Moon Ephemeris System. Dynamical Systems: An International Journal, Special Issue: Dynamical Systems in Dynamical Astronomy and Space Mission Design, **20**(1):149-173, March 2005.

18. A.E. Bryson and Y. Ho, Applied Optimal Control: Optimization, Estimation, and Control. Hemisphere Pub. Corp., New York, 1975.

19. McInnes, C. R., 1999, *Solar Sailing: Technology, Dynamics and Mission Applications* (United Kingdom: Praxis Publishing Ltd).

20. J.T. Betts, Practical Methods for Optimal Control Using Nonlinear Quadratic Programming. Society of Industrial and Applied Mathematics, Philadelphia, Pennsylvania, 2001.

21. J. T. Betts and S. O. Erb, "Optimal Low Thrust Trajectories to the Moon", SIAM Journal on Applied Dynamical Systems, **2**(2), pp. 144-170, May 2003.

22. J. T. Betts, "Very Low Thrust Trajectory Optimization Using a Direct SQP Method," Journal of Computational and Applied Mathematics, **120**(1-2), pp. 27-40, August 2000.

23. J. T. Betts, "Optimal Interplanetary Orbit Transfers by Direct Transcription," The Journal of the Astronautical Sciences, **42**(3), pp. 247-268, July-September 1994.

24. J. T. Betts, "Using Sparse Nonlinear Programming to Compute Low Thrust Orbit Transfers," The Journal of the Astronautical Sciences, **41**(3), pp.349-371, July-September 1993.

25. T. F. Coleman and Y. Li. On the Convergence of Reflective Newton Methods for Large-Scale Nonlinear Minimization Subject to Bounds. Mathematical Programming, 67(2):189–224, 1994.

26. T. F. Coleman and Y. Li. An Interior Trust Region Approach for Nonlinear Minimization Subject to Bounds. SIAM Journal on Optimization, 6:418–445, 1996.

27. Howell, K. C., and Pernicka, H. J., 1988, Numerical determination of Lissajous trajectories in the restricted three-body problem. Celestial Mechanics, 41, 107-124.

28. GILL, P.E., MURRAY, W., SAUNDERS, M.A., and WRIGHT, M.H., 'A Schur-Complement Method for Sparse Quadratic Programming,' Report SOL 87-12, Department of Operations Research, Stanford University.